

Toward Automated Fall Risk Assessment: Validation of an FMCW Radar-Based Timed Up and Go Test

Alexandre Bordat^{ID}, Claire Béranger^{ID}, Michel Chapron, Petr Dobias^{ID},
Julien Le Kernec^{ID}, Senior Member, IEEE, David Guyard, and Olivier Romain^{ID}

Abstract—Falls among the elderly present a significant health-care and socioeconomic challenge. The timed up and go (TUG) test is a widely used tool for assessing mobility and fall risk. However, traditional methods are limited in terms of objectivity and scalability. This study introduces a radar-based approach to automating the TUG test using frequency-modulated continuous-wave (FMCW) radar. The main objective is to provide an automated, nonintrusive, and privacy-preserving system for fall risk assessment through precise segmentation of TUG test phases (standing up, walking, turning around, and sitting down) and extraction of key gait parameters, such as walking speed, distance traveled, and phase durations. Validated against a cohort of 100 participants, the system achieved a mean relative velocity error of 8.89% and a mean absolute time error of 0.159 s. These results demonstrate high accuracy and robustness, making it a promising tool for fall risk assessment in both clinical and home environments. The strong correlation agreement for studied metrics (asymmetry and cadence) is confirmed by the intraclass correlation coefficient (ICC) between Motion Capture (MoCap) and radar, with $ICC_{\text{asymmetry}} = 81.7\%$ and $ICC_{\text{cadence}} = 76.2\%$. Additionally, the Bland–Altman analysis further supports this agreement, showing a strong concordance between the radar and MoCap measurements for both metrics.

Index Terms—Elderly fall estimation, gait analysis, human activity recognition, radar, real time.

I. INTRODUCTION

A. Falls in a Socioeconomic Context

IN FRANCE, the issue of falls among the elderly is a critical challenge that encompasses significant health, social, and economic dimensions. Drawing on epidemiological research by Thélot et al. [4], it is highlighted that falls are the primary cause of injury-related hospital admissions in this

Received 24 March 2025; revised 2 June 2025; accepted 23 July 2025.
Date of publication 30 July 2025; date of current version 19 August 2025.
(Corresponding author: Alexandre Bordat.)

This work involved human subjects or animals in its research. Approval of all ethical and experimental procedures and protocols was granted by the Research Ethics Committee of the CY Cergy Paris Université under Approval No. 202307-004 (October 11, 2023).

Alexandre Bordat is with the ETIS Laboratory UMR 8051, ENSEA, CNRS, CY Cergy Paris University, 95000 Cergy, France, and also with Bluelinea, 78000 Versailles, France (e-mail: alexandre.bordat@ensea.fr).

Claire Béranger, Michel Chapron, and Petr Dobias are with the ETIS Laboratory UMR 8051, ENSEA, CNRS, CY Cergy Paris University, 95000 Cergy, France.

Julien Le Kernec and Olivier Romain are with the ETIS Laboratory UMR 8051, ENSEA, CNRS, CY Cergy Paris University, 95000 Cergy, France, and also with the James Watt School of Engineering, University of Glasgow, G12 8QQ Glasgow, U.K.

David Guyard is with Bluelinea, 78000 Versailles, France.

Digital Object Identifier 10.1109/TRS.2025.3594236

demographic, with about 30% of individuals over 65 years old and 50% over 80 years old experiencing at least one fall annually. These falls not only lead to direct physical injuries, such as hip fractures requiring hospitalization and surgical intervention, but also have profound psychological impacts. The fear of falling again can lead to reduced mobility, social isolation, and a condition termed “post-fall syndrome,” characterized by a loss of confidence and heightened anxiety.

The healthcare system is strained by the increased emergency visits and prolonged hospital stays associated with falls. This raises healthcare costs significantly and places a heavy demand on rehabilitation services, including physiotherapy and occupational therapy, to restore mobility and independence [5]. Beyond the immediate healthcare costs, the economic implications of falls are extensive, covering long-term care needs, home adaptations, assistive devices, and the loss of productivity of the elderly and their caregivers. These aspects underline the comprehensive economic burden that falls impose on the healthcare system and society [6], [7].

To address this multifaceted issue effectively, it is necessary to implement effective fall prevention strategies that provide comprehensive healthcare and rehabilitation services and establish robust support systems. Such measures are essential to protect the well-being of elderly population and ensure the sustainability of the healthcare system and the broader economy [8].

B. Clinical Solutions for Fall Risk Assessment

Building on this foundation, the focus on geriatric healthcare underscores the necessity of accurately assessing fall risk among the elderly to enhance their well-being. The timed up and go (TUG) test is highlighted for its practicality and significant role in daily clinical settings due to its ease of use and quick administration. Alongside the TUG test, the Timetti Performance Oriented Mobility Assessment (POMA) and the functional reach test (FRT) are also recognized for their utility in evaluating balance and mobility, each with its own set of advantages for fall risk assessment [9], [10]. All their specific characteristics are summarized in Table I.

These assessment tools are crucial components of a comprehensive approach, allowing for early identification of individuals at risk and the implementation of tailored interventions to mitigate these risks [11].

The TUG test stands out for its simplicity and efficiency, making it a preferred option for balance assessment in

TABLE I
COMPARISON OF TUG TEST, TINETTI POMA, AND FRT

Aspect	Timed Up and Go (TUG) Test [1]	Tinetti Performance Oriented Mobility Assessment (POMA) [2]	Functional Reach Test (FRT) [3]
Purpose	Assess mobility and balance	Evaluate gait and balance	Measure stability and balance through reach
Components	Timed rise from a chair, walk 3 meters, turn, walk back, sit down	Gait assessment (e.g., step length, height) and balance assessment (e.g., sitting balance, standing up from chair)	Maximal forward reach while standing
Duration	Around 1-2 minutes	10-15 minutes	A few minutes
Equipment	Chair, stopwatch, tape measure (for distance)	Chair, stopwatch, measuring tape, various obstacles for gait section	Measuring tape or yardstick, wall
Scoring	Time taken to complete the task	Scoring based on multiple items; maximum score of 28	Distance reached in inches or centimeters
Interpretation	< 10s: normal; 10-20s: good mobility; > 20s: impaired mobility	Higher scores indicate better performance; scores below 19 indicate high risk of falls	< 6 inches: high fall risk; 6-10 inches: moderate fall risk; > 10 inches: low fall risk
Target Population	Older adults, individuals with mobility issues	Older adults, individuals with balance and gait issues	Older adults, individuals with balance issues
Advantages	Simple, quick, minimal equipment	Comprehensive assessment of gait and balance	Simple, minimal equipment, objective measurement
Limitations	May not detect subtle balance impairments	Longer to administer, requires more equipment	Only assesses forward reach, does not measure other directions of balance
Clinical Use	Screening for mobility problems, fall risk	Detailed balance and gait assessment for fall risk	Screening tool for balance issues, fall risk

resource-limited and/or time-constrained environments. It has shown a moderate correlation with the Tinetti POMA and can complement other clinical measures for a more accurate prediction of fall risks [5]. However, challenges exist, such as the need for trained personnel to administer the Tinetti POMA and the lack of comprehensive risk assessment when using the TUG test alone, suggesting the integration of additional tests for better predictive accuracy.

Concerns regarding the TUG test's objectivity and scoring consistency among clinicians have been raised, alongside its limited normative reference values for those under the age of 60. The incorporation of technology is proposed to enhance the test's objectivity and reduce subjectivity. Regular monitoring with the TUG test is essential for detecting mobility and balance changes over time, improving fall risk prediction [12].

This research emphasizes the TUG test's benefits, including its ease of integration into daily activities and clinical settings, minimal training requirements, and its quantitative assessment of mobility and balance. These features make the TUG test valuable for clinical diagnosis and monitoring patient's progress, advocating for its use in systematic fall risk assessments to facilitate proactive fall prevention in elderly care [13], [14].

C. Technological Solutions for Objective Measures of TUG Test

Recent technological advancements, particularly in sensor technology and computational methods, have significantly enhanced the precision of TUG test analysis. Studies have demonstrated the clinical value of instrumented TUG (iTUG)

test parameters, especially in terms of balance assessment. For instance, Caronni et al. [15] found that turn duration and vertical angular velocity during the TUG test are strong predictors of balance. Inertial sensors in mobile devices have further refined the TUG's measurement accuracy by capturing detailed parameters such as time duration, angular velocity, and step count, aiding in disease recognition and performance evaluation [16].

Depth sensors and machine learning algorithms have been used to identify behavioral parameters that distinguish between high and low fall risk individuals, focusing on metrics like sitting down speed and gait speed. However, depth sensors can sometimes lack the resolution needed for precise detection of small movements, which may affect the accuracy of fall risk assessments. Additionally, they can be sensitive to environmental conditions, such as strong lighting and reflective surfaces (e.g., mirrors), which can interfere with sensor readings and reduce reliability [11]. Research by Mangano et al. [17] on the use of single inertial sensors revealed that while healthy individuals of all ages performed similarly on the iTUG, older adults showed adaptive adjustments, particularly during turns, highlighting the complex nature of aging mobility.

Accelerometers are the most popular for fall risk assessment due to their portability and affordability, but their sensitivity to noise and drift often necessitates complex preprocessing. This increases system complexity and cost, while inadequate filtering risks losing critical data [18]. The accuracy of predictions using accelerometers is affected by signal quality, which can be compromised by improper synchronization or sensor placement. Measurements from unstable locations, like extremities,

TABLE II
COMPARISON BETWEEN CW AND FMCW RADAR

Criterion	CW Radar	FMCW Radar
Data Provided	Relative velocity (Doppler effect)	Relative velocity and precise distance information
Operating Principle	Continuous wave; measures frequency shift	Frequency-modulated chirps; measures both velocity and distance
Spatial Resolution	No direct distance measurement	High resolution for position detection
Multi-Target Detection	Limited differentiation based on distance	Differentiates targets by both distance and velocity
Applications	Fast object tracking, simple movements	Complex motion analysis, precise localization, multi-target tracking
Advantages	Simple, cost-effective	Detailed motion analysis, high precision

often increase variability and reduce analysis reliability [19]. Moreover, accelerometers frequently yield inconsistent results for parameters such as double support time, requiring better standardization. High false-positive rates also hinder accurate fall risk detection, underscoring the need for robust models and improved data interpretation [18], [19].

Video analysis for TUG test automation has emerged as a promising approach, offering the potential for remote patient monitoring without the need for specialized hardware. This method has been applied to automate TUG test subtask segmentation and streamline clinical workflows using conventional video cameras and computer vision techniques [20].

However, video-based approaches also raise privacy concerns, as patients may feel uncomfortable being continuously recorded, especially in home settings. Additionally, video-based methods face challenges with accuracy in uncontrolled environments, such as lighting variations and the need for precise camera positioning.

A first study [12] explored the use of a Doppler radar integrated into a chair to automate the TUG test, addressing privacy concerns and avoiding wearable sensors. This approach enabled the extraction of some gait parameters through radar signal analysis. The intrinsic limitations of continuous-wave (CW) radar systems, compared to frequency-modulated CW (FMCW) systems, hinder their ability to extract precise positional data. CW radar measures relative velocity using the Doppler effect but lacks the capability to track instantaneous radial positions or perform multiperson tracking. These constraints make it unsuitable for distinguishing multiple signatures or reliably separating TUG-related test activities from daily routines. To overcome these issues, FMCW radar was chosen for its ability to provide both velocity and high-resolution distance data. This enables precise characterization of motion phases and transitions during the TUG test. FMCW systems also allow detailed positional tracking and differentiation of multiple targets, making them essential for analyzing complex movements, detecting gait asymmetry, and ensuring robust performance in diverse environments.

As shown in Table II, FMCW radar demonstrates superior precision and adaptability for this application. Prior methodologies, such as clustering to separate noise from oscillatory signals [12], face challenges due to context-dependent noise patterns that limit generalizability. In contrast, FMCW radar offers both reliable and scalable solutions for fall risk assessment and fall detection [22], establishing itself as a robust

tool for improving TUG test analysis and overcoming the limitations of CW systems. Furthermore, due to the confusion between the radar and Vicon Motion Capture (MoCap) curves in [12, Fig. 12], the overall impression may be biased, potentially misleading the reader about their respective performances. This makes it appear as though the Vicon system, considered as the ground truth, performs worse than the radar, which is incorrect. Additionally, the choice to use clustering to separate noise from oscillation signals may have limitations, as noise can be highly contextual and influenced by the specific conditions of each recording environment. In real-world environments, noise sources and patterns may vary significantly, which may reduce the generalizability of model training based on noise characteristics from a controlled setting.

II. RELATED WORK

This section explores existing research on fall risk assessment methods, with a focus on the widely used TUG test. We examine its definition, clinical relevance, and how technological advancements have enhanced its precision. Additionally, we review sensor-based approaches that have been employed to automate and improve the accuracy of fall risk evaluations, highlighting both achievements and limitations in current methodologies.

A. Definition and Significance of the TUG Test

The TUG test [1] evaluates mobility and balance to assess fall risk. Participants stand up from a chair, walk 3 m, turn around, walk 3 m, turn around, and sit down, with the time taken recorded. A time of ≤ 10 s indicates normal mobility, a time between 11 and 20 s suggests moderate impairment, and a time of >20 s reflects severe impairment and high fall risk. Widely used for its simplicity and speed, the test benefits from technological enhancements for more objective assessments (see Fig. 1 for a visual representation).

The TUG test has been chosen as the foundation for automated fall risk assessment due to its instrumentable nature, allowing for the integration of technology to enhance objectivity. The incorporation of accelerometers, as highlighted in [23], demonstrates the value of adding gait characteristics like walking speed and turn duration to improve the sensitivity and predictive power of the test. This approach not only provides a richer analysis of balance and mobility but also addresses limitations inherent in traditional methods, thereby offering a more robust tool for identifying fall risk in populations prone to falls.

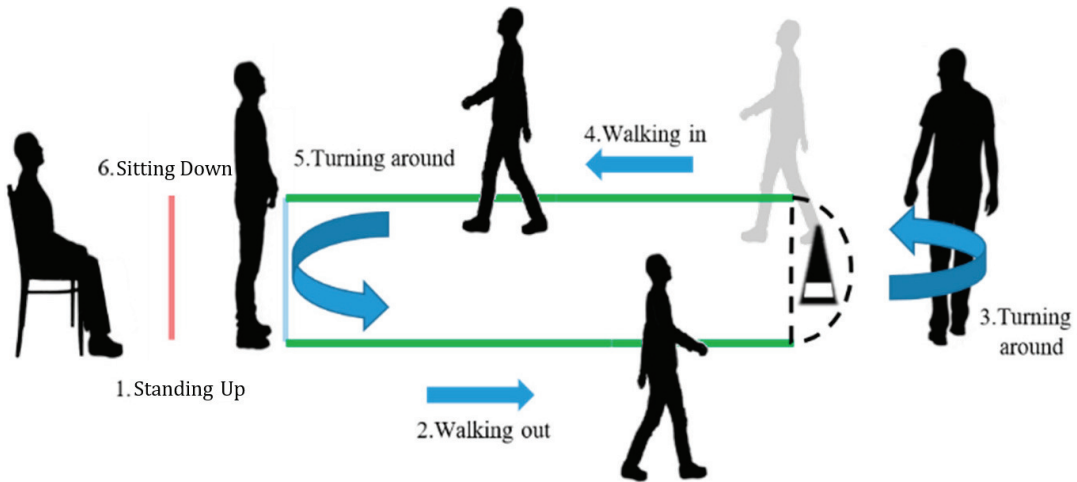


Fig. 1. Graph illustrating the phases of the TUG test, including standing up, walking, turning around, and sitting down and its associated spectrogram 3 and range-time 5 graph. Adapted from [21].

The features extracted from the TUG test, such as distance traveled, average forward speed, average return speed, and phase execution times, are well-established indicators for fall risk assessment. According to Greene et al. [24], these parameters are critical as they reflect core components of mobility, including gait stability, speed, and transitions between movements, which are often compromised in individuals at high risk of falls. For example, slower speeds and prolonged phase durations have been correlated with increased fall risk due to reduced functional mobility and balance control. These features are not only meaningful for clinical evaluation but are also readily obtainable using radar systems, enabling objective and continuous monitoring in diverse settings.

B. Related Work on Sensor-Based Fall Risk Assessment

In addition to the previously mentioned studies, Soubra et al. [12] introduce a novel system that automates the TUG test using an X-band Doppler radar (MDU1130) with a 9.9-GHz carrier frequency embedded in a chair's backrest. This system addresses privacy concerns associated with wearable sensors and camera-based systems, offering a contactless and nonintrusive solution. The radar output is amplified and filtered through a bandpass filter (5–500 Hz) to reduce noise and improve signal quality. An optoelectronic Vicon MoCap system with eight infrared cameras (Bonita 10) captures the 3-D positions of reflective markers on participants, serving as a reference for validating the radar-based measurements.

The signal processing methodology involves several key steps. First, the continuous wavelet transform (CWT) is employed to transform radar signals from the time domain to the time–frequency domain using the bump wavelet function, facilitating multiresolution analysis to extract speed signals of the torso and limb oscillations. Subsequently, torso speed signals are identified by locating the maximum energy distribution in the scalogram, while limb oscillations are distinguished from noise through a semi-supervised machine learning approach based on K -means clustering. Initial centroids for the K -means algorithm are derived from thresholds

established using baseline noise signals, and a morphological closing operation is applied to refine the clustering results.

TUG test phase segmentation involves identifying the first and last steps of walking to distinguish the transfer phase from the walking phase by detecting peaks and troughs in the torso speed signal. The DARC algorithm, introduced in [12], is used to detect the start and end of the turning-around phase by analyzing variance signals derived from the CWT matrix. From these segmented phases, 14 spatiotemporal gait parameters—including step length, stride length, gait cycle duration, swing time, cadence, and walking speed—are calculated based on detected peaks and their corresponding time indices. Although the radar system's parameters and phase segmentations show high correlation coefficients (r) with the Vicon system (e.g., $r = 0.8$ for torso speed signals and $r = 0.91$ for limb oscillations), the study does not fully address some challenges highlighted in related works. For instance, Ntanis et al. [25] used inertial measurement unit (IMU) and ultrawideband (UWB) sensors to evaluate TUG test parameters, demonstrating the potential of multisensor fusion but requiring wearable devices that could reduce user comfort. Similarly, Weiss et al. [23] enhanced fall risk detection with accelerometer-based systems but faced limitations due to sensor noise and calibration. Dubois et al. [27] employed the Microsoft Kinect to classify fall risks, emphasizing gait speed and step length but raising concerns about privacy and sensitivity to environmental conditions. These advancements in signal processing and system design offer a promising step toward continuous, unobtrusive monitoring of gait and balance in elderly individuals, but further work is needed to address these limitations and improve robustness in diverse application contexts.

Hadjipanayi and Constandinou [26] introduced a novel method utilizing UWB radar for remote gait analysis, focusing on joint range–Doppler–time representations to accurately extract spatiotemporal gait features. Their system demonstrated 90%–98% accuracy in estimating gait parameters and showed strong correlation with optical MoCap systems,

TABLE III
SUMMARY OF TUG TEST APPROACHES, RESULTS, AND LIMITATIONS

Reference	Approach	Key Results	Possible Limitations
Soubra <i>et al.</i> [12]	Doppler radar; CWT for signal processing; DARC for phase segmentation.	High correlation with Vicon ($r = 0.8$ and $r = 0.91$); 14 gait parameters extracted.	No distance measurement (CW radar); no asymmetry analysis; requires controlled settings.
Ntanis <i>et al.</i> [25]	IMU and UWB sensor fusion for gait analysis.	Accurate spatiotemporal parameters in controlled environments.	Multiple wearable devices reduce user comfort; no asymmetry analysis.
Hadjipanayi <i>et al.</i> [26]	UWB radar-based gait analysis using joint range-Doppler-time representation.	High accuracy (90–98%) in spatiotemporal gait parameter estimation, validated against optical motion tracking.	Limited applicability to short-range environments; less precise velocity tracking compared to FMCW; no asymmetry analysis.
Weiss <i>et al.</i> [23]	3D accelerometer on lower back; automated analysis of jerk, range, and gait speed.	87% accuracy for fall risk detection; independent mobility features captured.	Sensor placement sensitive; no asymmetry analysis; limited generalizability.
Dubois <i>et al.</i> [27]	Kinect sensor for depth-based monitoring; machine learning for gait features.	Perfect fall risk classification with two parameters; low-cost setup.	Environment-dependent; privacy concerns; no asymmetry analysis.

suggesting that UWB radar technology holds significant potential for unobtrusive, high-precision gait monitoring in both clinical and home environments. These advancements complement our work using FMCW radar, as both approaches emphasize the benefits of radar technology for noninvasive and continuous gait analysis.

These summaries are synthesized in Table III to facilitate the comparison of approaches, methodologies, and results of the different systems studied.

C. Limitations of Current Solutions and Technical Challenges

Despite significant progress, there remain areas for improvement in the automation of the TUG test. A critical aspect in characterizing movement involves not only measuring speed but also accurately determining the patient's position. One limitation is the use of CW radar, which does not provide instantaneous distance measurements, unlike FMCW radar.

Additionally, assessing fall risk through the measurement of asymmetry during the phases of the TUG test is a key criterion. *Asymmetry* refers to the unevenness in spatiotemporal gait parameters, such as step length, stance time, or swing time, between the two legs during walking. This unevenness is strongly correlated with fall risk, as evidenced by studies showing significant relationships between gait asymmetry and balance measures ($r = -0.36$ to -0.63) [28], [29], [30]. However, previous studies have not successfully automated the extraction of asymmetry in the TUG test, presenting another area needing enhancement.

These limitations highlight the need for advanced methodologies to enhance the accuracy and automation of the TUG test, paving the way for the following contributions introduced in this study.

- 1) A model of the TUG test in distance–time, featuring automatic segmentation of the TUG test phases (standing up, walking, turning around, and sitting down), is presented. Moreover, the model allows for the automatic extraction of crucial metrics, including the distance traveled, average forward speed, average return speed, and the execution times for each phase.

- 2) A model of the TUG test in velocity–time, featuring automatic extraction of several gait parameters, is discussed.
- 3) Measurements and automatic extraction of the asymmetry of the TUG test (which is strongly correlated with the risk of falling).

III. METHODOLOGY

In this section, we will briefly outline our previous contributions to the processing and classification chain. Following this, we will introduce the specific contributions of this article: range–time segmentation, velocity–time data extraction, and the detection of leg speed peaks in the velocity–time graph.

A. Our Previous Contributions to the Processing and Classification Chain

1) *Radar Data Acquisition:* In our earlier studies [16], [22], an FMCW radar system, model SDR 980AD2 from Ancortek, was used. This radar operates in the X band with a carrier frequency of 9.8 GHz, an instantaneous bandwidth of 400 MHz, and a chirp duration of 1 ms. This configuration enables the detection of indoor human activities with a Doppler frequency range of ± 500 Hz. These parameters provide a suitable Doppler frequency range of ± 500 Hz, facilitating the detection of indoor human activities [31]. The system features a single transmitting antenna and two receiving antennas, with a transmit power of +19 dBm. The two receiving antennas facilitate the measurement of the reflection's angle of arrival, which could be further exploited in future analyses. For down-conversion, the radar utilizes hardware dechirping (stretch processing), which involves mixing the received signal with the transmitted signal. The resulting downconverted signal, known as the beat frequency, is then low-pass filtered and amplified before digitization. The intermediate frequency (IF) signal consists of two channels, in-phase (I) and quadrature (Q), allowing for the capture of complex samples. The analog-to-digital converter (ADC) samples at a rate of 128 kHz, corresponding to 128 samples per 1-ms sweep. The radar's application programming interface (API) requires predefined

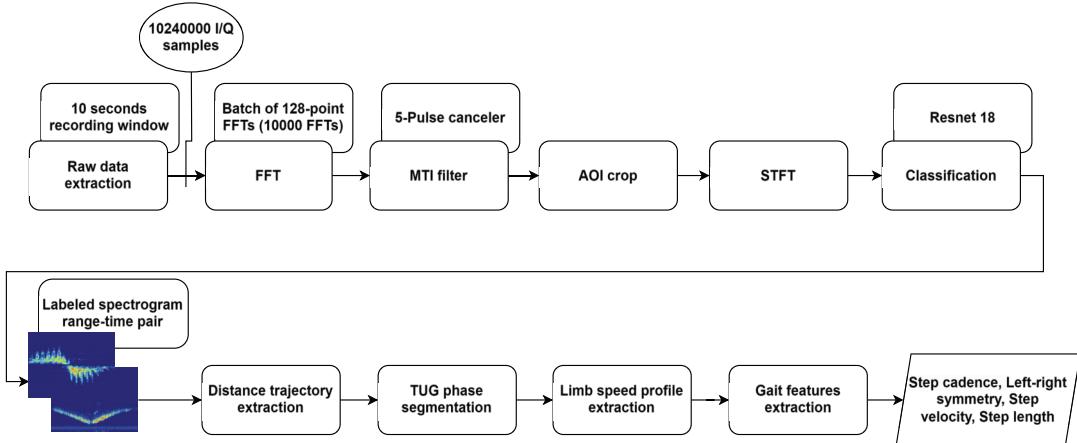


Fig. 2. Global processing chain.

recording lengths, with each session lasting 10 s. This duration is sufficient for capturing the specified activities.

2) *Data Preprocessing*: The preprocessing chain is divided into several subprocessing blocks as in Fig. 2. Initially, the input signal is interleaved and must be deinterleaved to retrieve the I/Q data from each antenna. The data are then formatted into a matrix of $128 \times M$, where 128 represents the number of time samples per chirp and M is the number of chirps for the activity record.

Next, the fast Fourier transform (FFT) of each received chirp is computed to determine the radial distance between the receiving antenna and the subject, as this distance is directly proportional to the beat frequency. The data are subsequently filtered using a five-pulse canceller applied along the slow-time dimension, serving as a moving target indicator to eliminate components near 0 Hz caused by stationary objects in the environment while preserving the integrity of the spectrogram.

A range bin from 5 to 25 (corresponding to 1.875–9.375 m) is selected, focusing on the range of target motion relative to the radar. This step, referred to as area of interest (AOI) crop, reduces processing time and minimizes noise in the calculation of temporal velocity signatures.

Finally, a short-time Fourier transform (STFT) is performed on the range-time data matrix using a Hamming window of 0.2 s with a 95% overlap. This extracts time-varying micro-Doppler features with a range resolution of 37.5 cm, a maximum measurable velocity of 7.65 m/s, and a Doppler resolution of 1.25 Hz (or 0.03 m/s).

This radar setup was selected due to its commercial availability and the need to validate the proposed methodology under real-world constraints. While the range resolution (~ 38 cm) is lower than what could be achieved with higher bandwidth or millimeter-wave (mmWave) radars, this tradeoff ensures robust performance in indoor environments. Future work will explore alternative configurations to improve resolution and noise reduction.

$$X(t, \omega) = \sum_{m=0}^{N-1} x[m] \cdot w[m-t] \cdot \exp(-i\omega m). \quad (1)$$

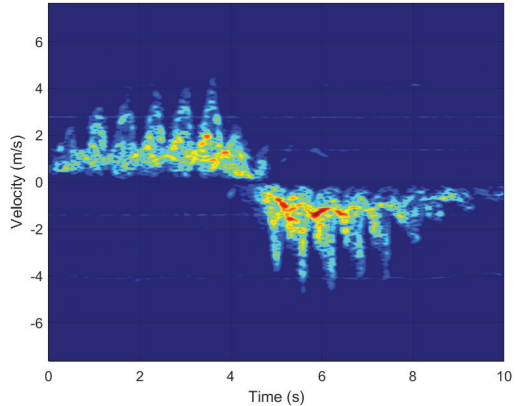


Fig. 3. Original velocity time graph (spectrogram).

Equation (1) represents the STFT, where $X(t, \omega)$ is the time-frequency representation of the signal, $x[m]$ is the input signal, $w[m-t]$ is the Hamming window function centered at time t , and $\exp(-i\omega m)$ is the complex exponential term. Here, m is the sample index, N is the total number of samples, ω is the angular frequency, and i is the imaginary unit. This transformation allows for the analysis of how the frequency content of the signal changes over time, providing detailed micro-Doppler features for velocity analysis and activity classification.

The output consists of data matrices representing the radial velocity of the target over time, allowing for the generation of images where the color indicates the varying amounts of energy received from the echoes by the receiving antennas in Fig. 3.

3) *Activity Classification*: In addition, a classification step has been developed to classify so-called daily activities. These activities are represented in the form of a spectrogram (data matrices representing the radial velocity of the target over time) and originate from the [32] database. Since the activities of standing up, sitting down, and walking can be correctly classified using a simple model like ResNet18, which initially yielded promising results [22], we hypothesize that the concatenation of these activities would lead to the correct

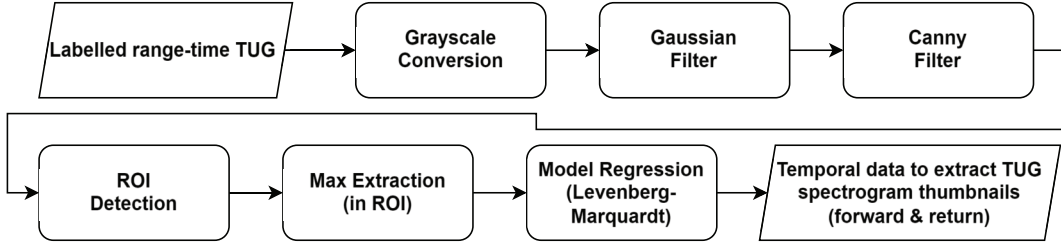


Fig. 4. Range time processing chain.

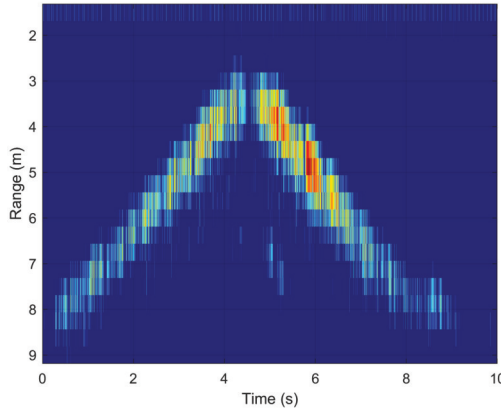


Fig. 5. Original range time graph.

classification of the TUG test activity. During this study, recordings involving human subjects were conducted [33] to validate the algorithms presented in this article. Informed consent was obtained from all participants prior to the collection of data, ensuring ethical¹ compliance with the study's protocol.

B. Range-Time Data Extraction

Post-classification, we specifically select the TUG test class for further analysis of the corresponding images. Processing range-time data is crucial for analyzing movements. Fig. 4 illustrates the range-time data processing chain used in this study.

1) *Max Extraction*: Once the RGB images are retrieved as in Fig. 5, they are converted to grayscale to simplify the following processing. A Gaussian filter is then applied to reduce residual noise

$$G(x, y) = \frac{1}{2\pi\sigma^2} \exp\left(-\frac{x^2 + y^2}{2\sigma^2}\right) \quad (2)$$

$$I'(x, y) = \sum_{i=-k}^k \sum_{j=-k}^k I(x-i, y-j) \cdot G(i, j). \quad (3)$$

Equation (2) defines the Gaussian filter $G(x, y)$, where σ is the standard deviation of the Gaussian distribution, and x and y are the spatial coordinates. Equation (3) describes the convolution of the grayscale image $I(x, y)$ with the Gaussian filter $G(i, j)$ to produce the filtered image $I'(x, y)$. Here, k is the size of the filter window, and the sums iterate over

¹The research experiments were approved by the Research Ethics Committee of the CY Cergy Paris Université on October 11, 2023 (Approval No. 202307-004).

the window dimensions. This process smooths the image by averaging pixel values with their neighbors, weighted by the Gaussian function, thus reducing noise.

After noise reduction, a Canny filter is used to extract image contours, corresponding to the radial distance of the person. By summing these contours line by line, we can automatically determine the spatial movement of the individual. The TUG test histogram, which follows a Gaussian distribution, is used to automatically identify AOIs within the image. From these areas, we extract the maximum grayscale value of each column, corresponding to the person's movement and store the (x, y) positions of these maximum values in a file

$$i_{\max(j)} = \arg \max_i A_{ij} \quad \forall j \quad (4)$$

$$(j, i_{\max(j)}) \quad \forall j. \quad (5)$$

Equation (4) defines $i_{\max(j)}$ as the index i of the image matrix A at which the maximum value of A_{ij} occurs for each column j .

Equation (5) represents the coordinates $(j, i_{\max(j)})$ of these maximum values for each column j . These coordinates correspond to the person's movement and are stored for further analysis.

Once the coordinates are obtained, we address columns lacking a maximum value in the AOI [(not a number (NaN) values)]. These NaN values are replaced with the value from the preceding column. If no preceding value exists (at the start of the image), the value from the first non-NaN column is used.

Our TUG test distance-time model is a nonlinear parametric model comprising several linear segments. The model's nonlinearity arises from the connection points between these segments. The initial segment is a horizontal line representing the standing up phase. The second segment, which is inclined with a positive slope, corresponds to the forward phase of the TUG test. The third segment, a horizontal line, represents the turning around phase. The fourth segment, inclined with a negative slope, corresponds to the return phase. Finally, the fifth segment, another horizontal line, represents the sitting down phase. Each segment is sequentially connected to the next one.

The model function is defined as follows:

$$f(x) = \begin{cases} y_1, & x \leq b_1 \\ y_1 + m_1(x - b_1), & b_1 < x \leq b_2 \\ y_1 + m_1(b_2 - b_1), & b_2 < x \leq b_3 \\ y_1 + m_1(b_2 - b_1) + m_2(x - b_3), & b_3 < x \leq b_4 \\ y_1 + m_1(b_2 - b_1) + m_2(b_4 - b_3), & x > b_4. \end{cases} \quad (6)$$

The model parameters include the connection points (b_1 – b_4), the initial height (y_1), and the slopes of the second and fourth segments (m_1 for the forward phase and m_2 for the return phase). This results in a total of seven parameters to be estimated for each regression.

The initial values for breakpoints b_1 and b_4 are chosen to represent a uniformly distributed TUG test (e.g., [175, 700] for a TUG test with 875 points). The maximum value of the TUG test is used to initialize breakpoints b_2 and b_3 , with the minimum abscissa of the max value assigned to breakpoint b_2 and the maximum abscissa of the max value assigned to breakpoint b_3 .

The initial plateau value, y_1 , which is one of the parameters, is extracted directly from the TUG test (the first value corresponding to the parameter). The initial slopes of the second and fourth segments are calculated as in (7) for the second segment (m_1) and as in (8) for the fourth segment (m_2)

$$(m_1)_{\text{init}} = \frac{\text{Max} - \text{Min}}{\text{minimum abscissa max} - 0} \quad (7)$$

$$(m_2)_{\text{init}} = \frac{\text{Min} - \text{Max}}{875 - \text{maximum abscissa max}}. \quad (8)$$

With all parameters initialized, we conducted a regression of the TUG test model using the Levenberg–Marquardt algorithm. The MATLAB’s default setting does not employ robust regression, which is suitable given the model’s precision and robustness, thus avoiding unnecessary processing time

$$S(\boldsymbol{\beta}) = \sum_{i=1}^n [y_i - f(x_i, \boldsymbol{\beta})]^2 \quad (9)$$

$$\boldsymbol{\beta}^{(k+1)} = \boldsymbol{\beta}^{(k)} - [\mathbf{J}^\top \mathbf{J} + \lambda \mathbf{I}]^{-1} \mathbf{J}^\top \mathbf{r}. \quad (10)$$

Equation (9) defines the sum of squared residuals $S(\boldsymbol{\beta})$, where y_i is the observed value, $f(x_i, \boldsymbol{\beta})$ is the model prediction, and $\boldsymbol{\beta}$ represents the parameter vector. Equation (10) describes the update rule for the parameter vector $\boldsymbol{\beta}$ in the Levenberg–Marquardt algorithm, where \mathbf{J} is the Jacobian matrix of partial derivatives, λ is the damping parameter, \mathbf{I} is the identity matrix, and \mathbf{r} is the residual vector. This iterative method refines the parameter estimates to minimize the sum of squared residuals.

After regression, we obtain data as in Fig. 6 and extract the optimized parameters corresponding to the expected values. These include the segmented phases of standing up, forward motion, turning around, return, and sitting down, identified via the breakpoints. Additionally, the average speeds during the forward and return phases are determined from the slopes.

We then segment the spectrogram images as in Fig. 7 (corresponding to the velocity–time images) to enhance the recognition of stable walking phases [forward phase as in Fig. 7(a) and return phase as in Fig. 7(c)]. This results in subimages corresponding to the phases of standing up, forward motion, turning around, return, and sitting down. In Fig. 7, the key observation is the extraction of subimages. If the detected phase corresponds to forward motion (positive velocity), the extracted subimage is highlighted in red; if it corresponds to the return phase (negative velocity), the extracted subimage is white. These phases of positive and negative velocity are identified based on the previous regression analysis, where the

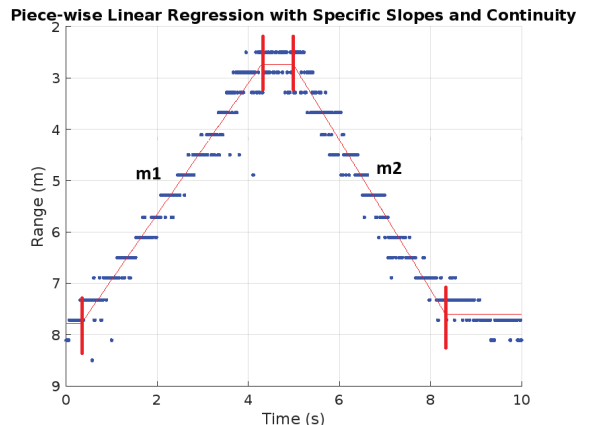


Fig. 6. Range time model.

average body velocity corresponds to the slope coefficients m_1 and m_2 . These graphs do not have axes, as we use the norm for image processing in this context.

C. Velocity–Time Data Extraction

The final phase involves cleaning and extracting the spectrograms (or speed–time profiles) of the TUG tests during stable phases as in Fig. 8. The processing chain includes several steps.

1) *Cleaning the Top and Bottom Bands:* The top and bottom bands of the image are cleaned to reduce noise. This is achieved by setting the red and green channels to zero and the blue channel to 131 for the top and bottom 10 rows of the image. It corresponds to the lower bound of the intensity scale in the colormap (Jet in MATLAB), which is mapped to the noise floor, defined as 35 dB below the strongest signal in the spectrogram. This ensures that only meaningful signals are retained while suppressing most background noise.

2) *Opening (Erosion and Dilation):* An opening operation, consisting of an erosion followed by a dilation, is applied to the blue channel of the image using a symmetric rectangular structuring element with a width of 7 pixels and a height of 3 pixels. This step helps to remove small noise elements and further emphasizes the primary activity area.

The mathematical representation of the opening operation is given by

$$A \circ B = (A \ominus B) \oplus B \quad (11)$$

where A is the image and B is the structuring element. Equation (11) describes the opening as an erosion (\ominus) followed by a dilation (\oplus).

The *erosion* operation is defined as

$$(A \ominus B)(x) = \min_{b \in B} \{A(x+b)\} \quad (12)$$

which means that for each position x , the minimum value of the image A within the neighborhood defined by the structuring element B is selected.

The *dilation* operation is defined as

$$(A \oplus B)(x) = \max_{b \in B} \{A(x-b)\} \quad (13)$$

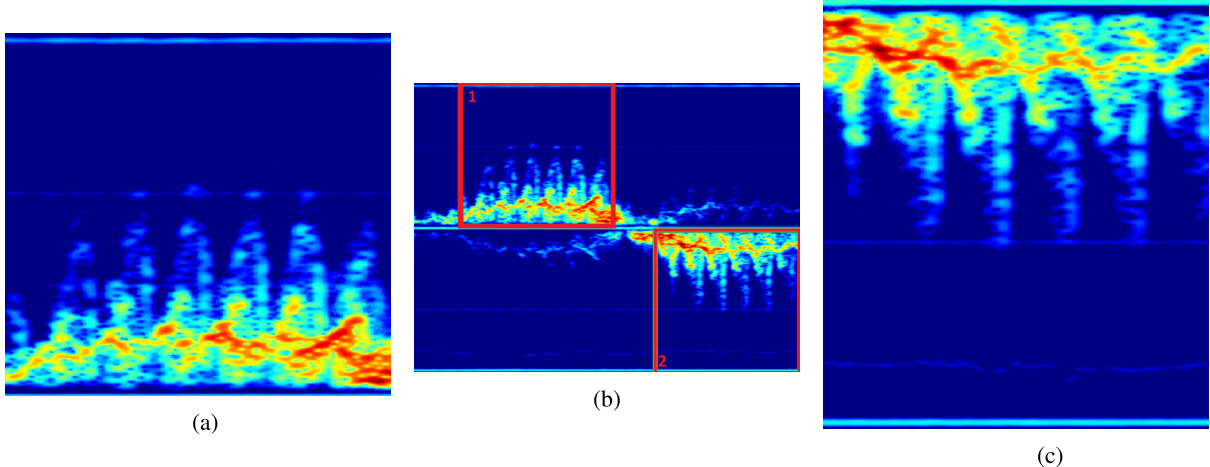


Fig. 7. Velocity time TUG test comparisons. (a) Velocity time TUG test outbound phase (red box). (b) Velocity time TUG test. (c) Velocity time TUG test return phase (white box).

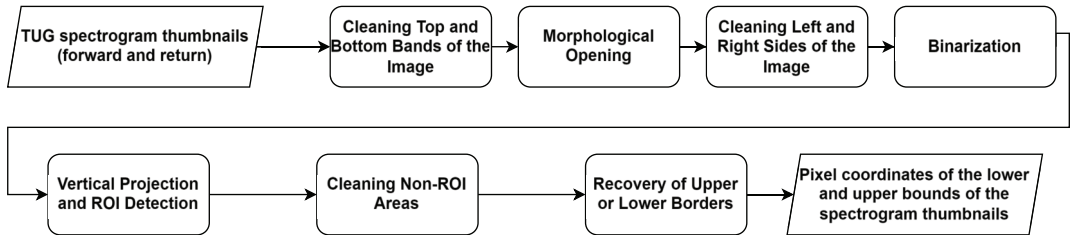


Fig. 8. Velocity time processing chain.

which means that for each position x , the maximum value of the image A within the neighborhood defined by the structuring element B is selected.

The erosion and dilation operations are inspired by [34] and [35], which highlight the use of morphological techniques in image processing.

The choice of a symmetric rectangular structuring element was made to address the specific nature of the noise present in the spectrograms. The noise typically appeared as long vertical lines. By using a symmetric rectangular structuring element, we were able to more effectively target and eliminate these vertical noise patterns without compromising the integrity of the primary activity structures in the image.

3) *Cleaning the Left and Right Sides:* The left and right sides of the image are cleaned after the morphological operations. The first and last columns of the image are set to a specific value to ensure that the edges do not contain noise, thereby preventing edge artifacts.

4) *Binarization:* The image is binarized as in Fig. 9(a) by setting pixels in the blue channel with the value 131 to black (0) and all other pixels to white (255). This binarization step creates a clean binary image that represents the primary activity area.

5) *Vertical Projection and Detection of Region of Interest:* The vertical projection of the binary image is calculated to determine the region of interest (ROI). This involves summing the number of nonzero pixels in each row and analyzing the resulting profile to identify where the primary activity is concentrated.

6) *Cleaning the Non-ROI Area:* Based on the vertical projection, it is determined whether the primary activity is located at the top or the bottom of the image. Depending on this detection, the non-ROI part of the image is cleaned. If the activity is at the top, the bottom third of the image is cleaned by setting the red and green channels to zero and the blue channel to 131 as in Fig. 9(c). If the activity is at the bottom, the top third is similarly cleaned.

7) *Extraction of the Activity Borders:* The borders of the primary activity are then recovered as in Fig. 9(b). If the activity is detected at the top, the first nonzero pixel in each column is identified and marked in the output image. If the activity is at the bottom, the last nonzero pixel in each column is identified and marked. This process extracts the contour corresponding to the legs, with each extracted value representing the leg speed at each instant.

The important aspect to observe in Fig. 9 is the effect of the processing applied to Fig. 9(c) compared to Fig. 7(c). It can be seen that the noise, particularly the mostly horizontal lines, has been effectively removed thanks to the previous processing steps. Another key observation is the extraction of the contour in Fig. 9(b) from the binarized image in Fig. 9(a), which corresponds to the leg velocity. Additionally, for consistency with image processing norms, no axes have been used in these figures.

D. Detection of Leg Speed Peaks in Velocity-Time Graph

The boundary data extracted from Fig. 9(b) consist of pixel values representing edges within the image. To make these

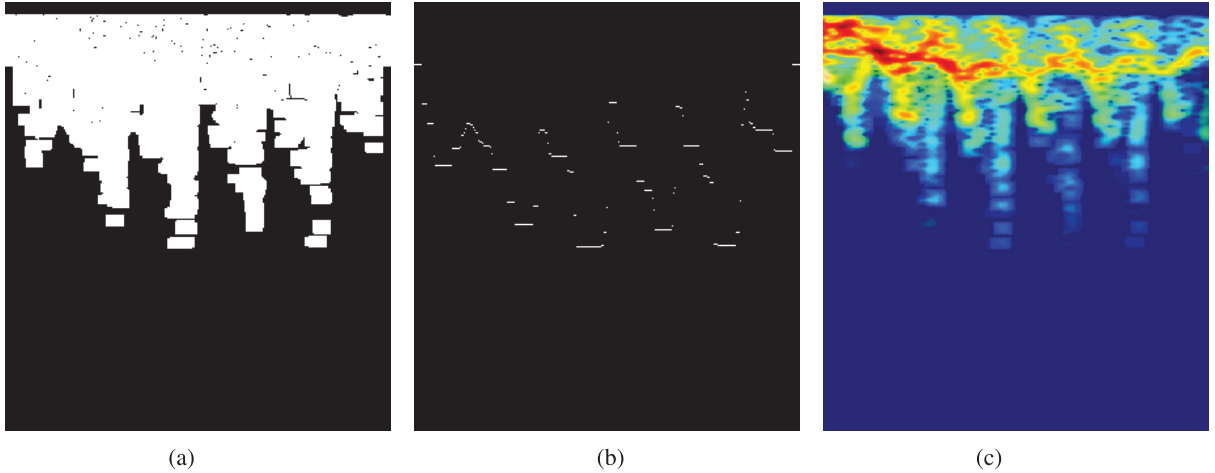


Fig. 9. Velocity time processing chain comparisons. (a) Velocity time binarization. (b) Velocity time contour. (c) Velocity time cleaned image.

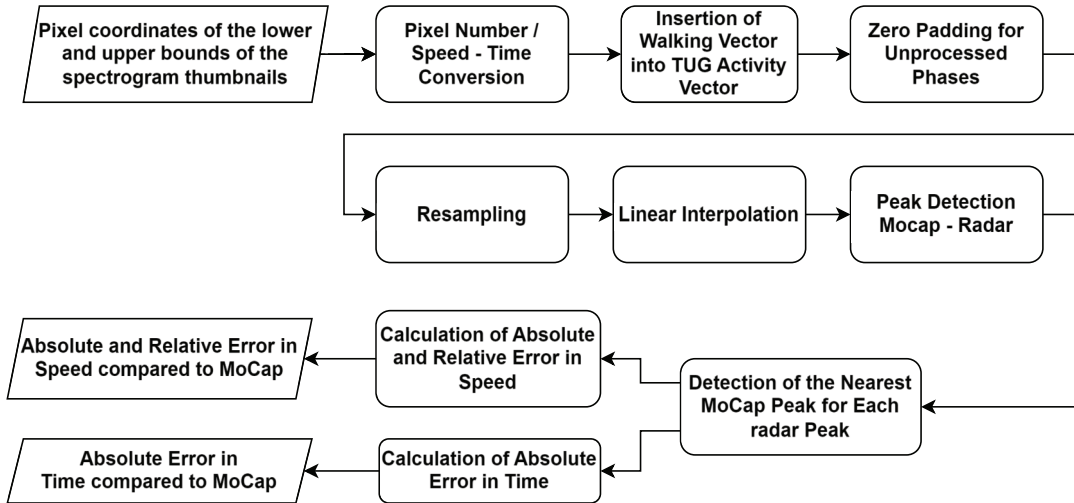


Fig. 10. Peak detection chain and error calculation.

values comparable to real-world measures such as speed (m/s) and time (s), a conversion is necessary. This conversion allows for direct comparison with MoCap data. The pixel-to-real-world conversion is performed in the first block of Fig. 10, which builds on the final block of Fig. 8. Specifically, pixel coordinates are transformed into velocities and time intervals.

Once the walking phase vectors are converted into their respective real-world units, they are reinserted into a time vector of length 875, corresponding to the original length of the time axis in the experiment. Both forward and backward walking phases are placed in the appropriate positions within this vector based on the segmentation timestamps of each phase.

To account for unprocessed phases, namely the standing up, turning around, and sitting down phases, zero padding is applied to the portions of the vector where these phases occur. This ensures that only the relevant walking phases are analyzed while maintaining the integrity of the entire time series.

1) Resampling and Interpolation: In order to synchronize the radar data with the MoCap data, it is necessary to resample the radar data. The MoCap data are recorded at 100 Hz over

a period of 10 s, yielding a total of 1000 data points. Thus, the radar data are resampled to match this number of points, ensuring temporal alignment with the MoCap system.

Following the resampling, linear interpolation is applied to the radar data to fill any gaps caused by the resampling process. This interpolation minimizes discrepancies between the radar and MoCap datasets, reducing the error associated with missing or irregular data points and providing a smoother comparison.

2) Peak Detection and Gait Analysis: Once the resampled radar and MoCap data are aligned, peak detection is performed to identify the points of maximum velocity during each leg swing phase. The peak detection algorithm is mathematically formulated in (14). Peaks correspond to the highest speed achieved during each walking phase, which allows for further analysis of gait characteristics.

From the detected peaks, several key gait parameters can be extracted, including stride cadence, number of strides, leg swing velocity, and other walking dynamics. These metrics provide valuable insight into the overall gait pattern and are essential for the comparison between radar and MoCap data.

3) *Equation for Peak Detection:* A peak at position i in a signal x is defined by the following combined conditions:

$$\begin{aligned} &x[i-1] < x[i] > x[i+1] \quad (\text{signal value at position } i) \\ &\text{and } x[i] \geq h_{\min} \quad (\text{minimum height } h_{\min} \text{ of the peak}) \\ &\text{and } |i-j| \geq d_{\min} \\ &\quad (\text{minimum distance } d_{\min} \text{ between peaks } i \text{ and } j) \\ &\text{and } \text{prominence}(x[i]) = x[i] - \min(x[l], x[r]) \geq p_{\min} \\ &\quad \text{minimum prominence } p_{\min} \text{ of the peak.} \end{aligned} \quad (14)$$

The list of variables used in (14) is given as follows.

- 1) $x[i]$: Value of the signal at position i (potential peak).
- 2) $x[i-1], x[i+1]$: Values of the signal at positions $i-1$ and $i+1$ (neighbors of $x[i]$).
- 3) h_{\min} : Minimum height required for the peak.
- 4) d_{\min} : Minimum distance required between two peaks.
- 5) $\text{prominence}(x[i])$: Prominence of the peak at position i , defined as the difference between the peak and the lower of the neighboring valleys.
- 6) $x[l], x[r]$: Values of the signal at positions l and r , representing the valleys to the left and right of the peak.
- 7) p_{\min} : Minimum prominence required for the peak.

Note: This algorithm is also used for valley detection by inverting the signal when it is positive. By applying the same conditions to the inverted signal, valleys can be identified using the peak detection criteria.

E. Step Time, Cadence, and Gait Asymmetry Calculation

To extract the step times, we first identify the valleys in the radar signal, corresponding to the moments when the foot contacts the ground during the gait cycle. The step times are then computed as the time differences between consecutive valleys

$$T_{\text{step}}^{(n)} = t_{\text{valley}}^{(n+1)} - t_{\text{valley}}^{(n)} \quad (15)$$

where $T_{\text{step}}^{(n)}$ represents the step time between the n th and $(n+1)$ th valley and $t_{\text{valley}}^{(n)}$ is the timestamp of the n th valley.

1) *Cadence Calculation:* Cadence, defined as the number of steps per minute, is calculated based on the total number of detected steps and the duration of the walking sequence. The cadence is computed as follows:

$$C = \frac{N_{\text{steps}}}{T_{\text{duration}}} \times 60 \quad (16)$$

where N_{steps} is the total number of steps detected and $T_{\text{duration}} = t_{\text{valley}}^{(N_{\text{steps}})} - t_{\text{valley}}^{(1)}$ represents the total duration of the walking sequence in seconds. The result is expressed in steps per minute.

2) *Gait Asymmetry Calculation:* To analyze gait asymmetry, the extracted step times are divided into two groups corresponding to alternating legs. The odd-indexed step times represent one leg (e.g., left leg), and the even-indexed step times represent the opposite leg (e.g., right leg)

$$T_{\text{odd}} = \left\{ T_{\text{step}}^{(1)}, T_{\text{step}}^{(3)}, T_{\text{step}}^{(5)}, \dots \right\} \quad (17)$$

$$T_{\text{even}} = \left\{ T_{\text{step}}^{(2)}, T_{\text{step}}^{(4)}, T_{\text{step}}^{(6)}, \dots \right\}. \quad (18)$$

The gait asymmetry is computed by comparing the temporal differences between alternating steps. To ensure consistency, both sequences are truncated to the same length, N , representing the minimum number of available steps between the two legs. The asymmetry for each step pair is calculated as follows:

$$A_i = \left(\frac{\left| T_{\text{odd}}^{(i)} - T_{\text{even}}^{(i)} \right|}{\frac{1}{2} (T_{\text{odd}}^{(i)} + T_{\text{even}}^{(i)})} \right) \times 100 \quad (19)$$

where A_i is the asymmetry percentage for the i th step pair, $T_{\text{odd}}^{(i)}$ is the step time for the odd (e.g., left) leg, and $T_{\text{even}}^{(i)}$ is the step time for the even (e.g., right) leg.

The final asymmetry metric is represented as the mean asymmetry across all N step pairs

$$A_{\text{mean}} = \frac{1}{N} \sum_{i=1}^N A_i. \quad (20)$$

This metric quantifies the temporal imbalance between the two legs, expressed as a percentage, with higher values indicating greater gait asymmetry. Both cadence and asymmetry are key indicators in gait analysis and fall risk assessment.

F. Error Calculation Methodology

To evaluate the performance of the radar-based gait analysis, the detected peaks are compared against the reference peaks from the MoCap system. The first step in this error analysis is to match each detected radar peak with its nearest corresponding peak from the MoCap data. This process is repeated for all peaks across all trials of the TUG tests.

Once the peaks are matched, two types of errors are computed in parallel. The first is the absolute error in the timestamps of the matched peaks, calculated as the difference between the radar peak timestamp and the corresponding MoCap peak timestamp. This error reflects the temporal alignment between the two systems.

The second metric is the relative velocity error for each detected peak. It is computed by taking the absolute difference between the velocities of the matched peaks (radar and MoCap) and dividing it by the velocity of the reference MoCap peak. This yields a percentage error that quantifies the deviation in instantaneous foot velocity between the two systems.

In addition to these pointwise errors, we assess the overall agreement between the radar-based system and the reference MoCap system using two complementary statistical methods: the intraclass correlation coefficient (ICC) and Bland–Altman analysis.

The ICC is a reliability metric that quantifies how closely repeated measurements—from different systems or raters—agree. It is particularly suitable for continuous measurements and accounts for both correlation and absolute agreement. In our context, where the same participants are recorded simultaneously by radar and MoCap, and we aim to assess whether both methods yield similar values for each subject, we adopt the ICC(2,1) model [36]. This model corresponds to a two-way random-effect formulation for absolute agreement on single measurements and is appropriate

when methods are treated as fixed and subjects are randomly sampled.

The ICC(2,1) is calculated as

$$\text{ICC}(2, 1) = \frac{\text{MS}_R - \text{MS}_E}{\text{MS}_R + (k - 1)\text{MS}_E + \frac{k(\text{MS}_C - \text{MS}_E)}{n}}$$

where MS_R is the mean square for rows (subjects), MS_C is the mean square for columns (methods), MS_E is the mean square the residual error, k is the number of methods ($k = 2$), and n is the number of subjects. An ICC close to 1 indicates excellent agreement; values below 0.5 indicate poor reliability. This coefficient quantifies the consistency of radar-based measurements with MoCap values across the population.

In parallel, the Bland–Altman method provides a graphical representation of agreement by plotting the difference between the two methods against their average. This analysis reveals any systematic bias and visualizes the dispersion of the differences. The limits of agreement (LoAs) are defined as the mean difference ± 1.96 times the standard deviation of the differences. A narrow LoA and a bias close to zero suggest strong agreement and interchangeability of the two methods for the given metric.

Together, these statistical methods provide a robust framework for assessing the reliability and validity of the radar-based gait analysis system compared to the gold standard MoCap.

G. Validation Data and Equipment

The validation dataset consists of recordings from 100 participants aged between 18 and 60 years. The sample is balanced in terms of gender and age: 50% male and 50% female, with 50% of participants in the 18–40 age group and 50% in the 41–60 age group. Each participant performed the TUG test three times under identical conditions.

None of the participants reported any known clinical condition that could lead to injury during the recorded activities, in accordance with the eligibility criteria approved by the institutional ethics committee.

MoCap data were acquired using a Vicon system composed of ten Vero cameras, synchronized via a dedicated Vicon Lab device. Data collection was triggered by a pressure sensor embedded in the seat, which activated both the radar and MoCap recordings when the participant initiated the standing movement. The radar system was placed directly in front of the chair at a distance of 6.5 m, allowing participants to walk toward and away from the sensor during the forward and return phases of the TUG test. The recorded MoCap data include the instantaneous velocity of the participants' ankles along the radar's radial axis. These data are exported as comma-separated value (CSV) files for further processing and analysis.

In total, the dataset comprises $100 \times 3 \times 2$ spectrogram images representing TUG test movements and an additional $100 \times 3 \times 2$ time–distance images representing participants' trajectories.

Population details are provided in Table IV, while performance metrics of the radar-based analysis—including average relative velocity error and absolute time error—are

TABLE IV
POPULATION CHARACTERISTICS

Category	Value
Participants	100
Age	50% (18–40), 50% (41–60)
Gender	50% M, 50% F for each age group
Weight	
Underweight	4%
Normal	56%
Overweight	33%
Obesity	7%
Sedentariness	69%
Activity	48%

summarized in Tables V and VI, along with their mean and median values.

IV. EXPERIMENTAL RESULTS

A. Error Metrics in Comparison to Ground Truth Data

In this section, we present the error analysis of our data extraction algorithm based on radar-generated data [33].

Furthermore, Tables V and VI report the ICC values between MoCap and radar for both cadence and asymmetry. The ICC assesses the *degree of consistency and absolute agreement* between the two measurement methods across different subjects. A high ICC indicates that the variations observed between the two modalities are primarily due to actual differences between subjects rather than measurement noise or inconsistencies. Specifically, the ICC values related to range-derived metrics are presented in Table V, while those related to velocity-derived metrics appear in Table VI. Typically, ICC values above 0.70 are considered good, while values between 0.50 and 0.70 are interpreted as moderate [36]. Here, the majority of the reported ICC values are above 0.70, indicating a good level of agreement between the two measurement methods. Furthermore, the associated p-values for ICC(2,1), which test the null hypothesis that the agreement is due to chance, are sufficiently low to conclude that the radar-based measurements can be considered statistically reliable.

By carefully examining these results, we can assess the effectiveness of our radar-based data extraction algorithm and its precision in capturing the participants' movements during the TUG test.

As shown in Fig. 11, the results from the peak extraction algorithm demonstrate its ability to accurately identify key features within the radar-generated data. The algorithm effectively captures significant motion events, such as changes in ankle velocity, which are critical for the TUG test analysis.

The Bland–Altman plots [Fig. 12(a) and (b)] illustrate the agreement between MoCap and radar measurements for both cadence and asymmetry metrics. The bias is close to zero, and the data points are fairly evenly distributed around the bias line, without any apparent systematic trend. Additionally, the majority of points fall within the LoAs, suggesting that the two methods provide comparable results with minimal systematic error. Importantly, zero falls within the 95% confidence interval (indicated by the green dashed lines) of the mean bias, indicating that the bias is not statistically significant according to Bland–Altman analysis recommendations [37].

TABLE V
ERROR METRICS FOR DISTANCE-TIME GRAPH

Metric	ICC (95% CI, p-value)	Mean Relative Error
Total TUG Time	94.5% [0.9300–0.9600], $p = 2.21 \times 10^{-139}$	2.76%
Forward Time	72.0% [0.650–0.790], $p = 1.2 \times 10^{-35}$	6.70%
Return Time	68.0% [0.600–0.750], $p = 2.8 \times 10^{-28}$	7.10%
Forward Speed	86.1% [0.8200–0.8900], $p = 6.49 \times 10^{-73}$	4.60%
Return Speed	83.9% [0.7900–0.8800], $p = 4.53 \times 10^{-58}$	4.36%
Average Turnaround Speed	72.0% [0.600–0.820], $p = 5.7 \times 10^{-30}$	8.80%

TABLE VI
ERROR METRICS FOR VELOCITY-TIME GRAPH

Metric	Value
Mean Relative Velocity Error	8.89%
Median of Global Mean Relative Error	8.04%
Mean Absolute Time Error	0.159 s
ICC between MoCap and radar for asymmetry	81.8% [95% CI: 0.75–0.87], $p = 2.89 \times 10^{-29}$
ICC between MoCap and radar for cadence	76.2% [95% CI: 0.65–0.85], $p = 2.50 \times 10^{-25}$

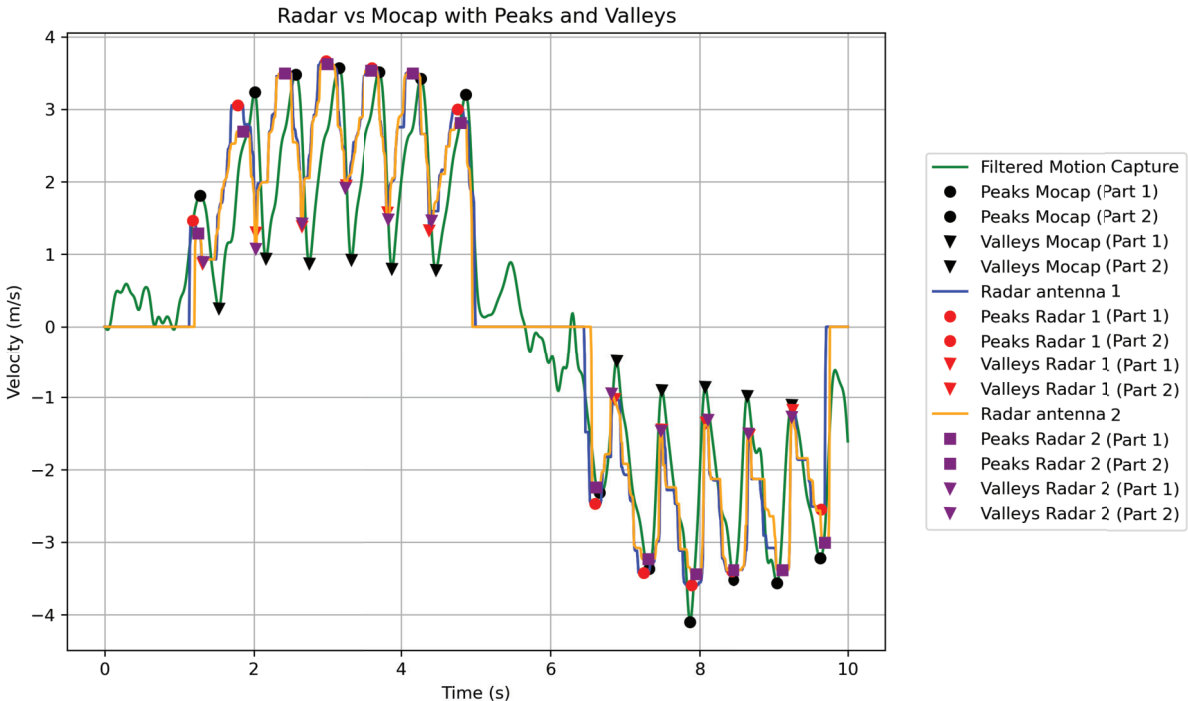


Fig. 11. Peak radar/MoCap extraction result.

V. DISCUSSION

In this study, we implemented an FMCW radar system to automatically segment and analyze the phases of the TUG test, extracting advanced gait parameters for fall risk evaluation in older adults. Our findings were compared to a recent study [12], which utilized a Doppler radar system embedded in a chair to automate the TUG test. Although both systems have shown promise in automated gait analysis, our methodology demonstrates several advantages in terms of accuracy, robustness, and comprehensiveness, which will be further discussed.

A. Data Acquisition Methodology

Our study employed an FMCW radar, known for its superior precision in detecting both the speed and position of

participants throughout the test. The multidimensional capabilities of the FMCW radar allow for a more detailed analysis of small movements, particularly subtle oscillations and postural shifts, which can be early indicators of mobility issues. This contrasts with the system used by Soubra et al. [12], who implemented a Doppler radar system. While innovative and less intrusive, Doppler radar is inherently limited in its ability to detect fine-grained positional changes, particularly over shorter distances. Doppler radar primarily provides velocity information, whereas FMCW radar can deliver both speed and highly accurate positional data, offering a richer dataset for assessing subtle gait variations.

Additionally, in comparison to a simple CW radar, which is mainly focused on measuring velocity but lacks distance information, FMCW radar stands out for its capacity to

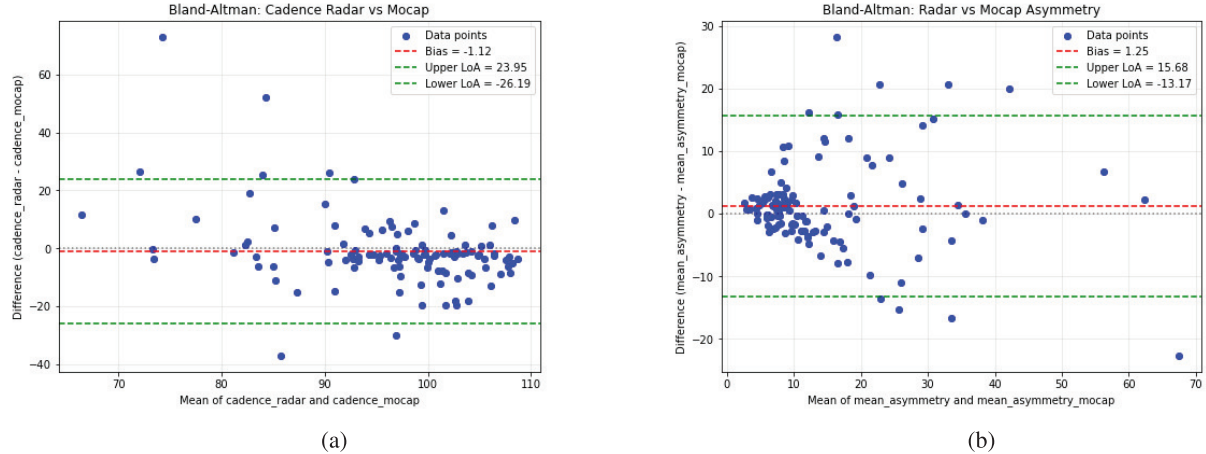


Fig. 12. Bland–Altman analysis of velocity-related gait parameters. (a) Cadence. (b) Asymmetry.

measure distances with precision. This is achieved through the frequency modulation of the transmitted signal, allowing it to capture both distance and velocity data simultaneously. The ability to measure distance makes FMCW radar particularly valuable in detecting detailed positional shifts, which are crucial for thorough gait analysis and fall risk evaluation.

Rationale: Our selection of FMCW radar is justified by its superior precision, especially in detecting micro-Doppler effects and minute movements, as well as its enhanced ability to measure both distance and velocity compared to a simple CW radar. These capabilities make FMCW radar a more suitable tool for comprehensive gait analysis, enabling a more accurate assessment of fall risk in elderly populations.

B. Phase Segmentation of the TUG Test

Our segmentation approach, using advanced and efficient algorithms such as the FFT and STFT, demonstrated superior robustness in accurately differentiating the phases of the TUG test (standing up, walking, turning around, and sitting down). This precision is crucial for identifying potential gait abnormalities that may be missed by more simplistic segmentation methods. In comparison, the segmentation approach of Soubra et al. [12] relied on a semi-supervised machine learning technique based on limb oscillations detected through Doppler radar signals. While functional, their method could lack the accuracy needed during complex phases, such as turning around or standing up transitions, due to the limitations of the Doppler radar in accurately capturing rapid directional changes.

Rationale: Our use of FFT and STFT allows for finer phase discrimination, particularly in complex movements like turns, which are often challenging for simpler methods. This approach enhances the reliability of the analysis and ensures that no critical phase is overlooked.

C. Gait Parameter Extraction

Our study extracted detailed gait parameters, which are critical indicators of fall risk. Although Soubra et al. [12] also extracted basic gait parameters, including cadence and

step length, their system does not account for more complex movement patterns, such as variations in walking speed during different phases. Our system's ability to capture data in both forward and backward directions allows us to easily and robustly compute key metrics, including step length, cadence, and walking speed, with enhanced precision and reliability. As detailed in Section III-C.1, our system operates with a signal threshold set at 35 dB, corresponding to the value 131, to ensure a reliable extraction of gait parameters while mitigating the impact of noise. This threshold was selected based on empirical observations to balance signal clarity and robustness in different walking conditions. Future studies will investigate the sensitivity of this parameter and its potential impact on the accuracy of gait parameter extraction, particularly in more variable environments or for individuals with altered mobility patterns. Furthermore, future studies are planned to specifically include older and clinically at-risk populations, with subgroup analyses to evaluate the generalizability and robustness of the extracted gait parameters across diverse cohorts.

Rationale: The extracted data will allow us to calculate these metrics efficiently and with robustness, providing a more comprehensive and accurate evaluation of a participant's mobility and fall risk.

D. Precision and Validation

Our system was validated using a large and diverse population, ensuring that the extracted parameters are robust across a variety of conditions. This contrasts with the study by Soubra et al. [12], which was validated on a smaller sample size of 26 subjects. While their system demonstrated high correlation coefficients with a reference system (e.g., Vicon), the generalizability of their results may be limited by the small sample size. In contrast, our validation with a larger dataset enhances the external validity of our findings, supporting the applicability of our system to a broader population, including individuals at higher risk of falls.

Rationale: Our study's robustness is further reinforced by the validation on a larger dataset. This not only improves the reliability of our results but also ensures that our system can be applied to a wider demographic, making it highly relevant for

both clinical and home-based assessments of mobility. While the error metrics provide valuable insights, their influence on real-world performance, particularly in less controlled environments, remains uncertain at this stage. Future work will focus on testing in clinical settings and specialized workshops under semiautomated conditions, followed by fully automated trials in home environments. These phases will help assess the system's robustness and adaptability to varying conditions, offering a clearer understanding of its real-world applicability.

E. Ethical Considerations and Privacy Protection in Radar-Based Monitoring Systems

Our radar-based monitoring technology addresses key ethical concerns related to continuous home surveillance by ensuring privacy and data security. Unlike visual monitoring systems, the radar operates without capturing images from the visible spectrum and can be discreetly installed behind thin walls, minimizing the feeling of intrusion [38]. All raw data are processed locally on the device, and once analyzed, the raw data are immediately deleted. Only essential activity information, such as movement patterns or critical events, is transmitted to the patient's medical record. This approach safeguards patient privacy, aligns with data minimization principles, and ensures that sensitive information is handled ethically and securely.

VI. CONCLUSION

This study presents a significant advancement in the automation of the TUG test using a radar-based system. By employing an FMCW radar, the study enhances the accuracy and comprehensiveness of fall risk assessments, particularly for elderly individuals. The proposed system successfully segments the TUG test phases (standing up, walking, turning around, and sitting down) and extracts essential gait parameters such as walking speed, step length, and cadence, making it a powerful tool for detecting mobility issues. Given its fine motion analysis capabilities, this device could also be utilized in other applications, such as measuring the improvement in gait for individuals recovering from an accident.

Compared to previous approaches relying on Doppler radar systems, this method offers superior precision in detecting both speed and position, providing more detailed insights into participants' movements. These results underline the potential of radar-based systems for nonintrusive, continuous monitoring in both clinical and home settings, contributing to improved elderly care and fall prevention strategies.

Our future work will focus on real-time processing using the Jetson platform's GPU, which is optimized for our previous FMCW radar processing chain. The focus will be on optimizing the algorithms applied after the STFT, as they represent computationally intensive steps in the processing pipeline. These include tasks such as micro-Doppler feature classification and extraction, which require significant computational resources for real-time analysis. This work aims to enhance system precision while maintaining efficiency for deployment in diverse clinical or home environments.

REFERENCES

- [1] D. Podsiadlo and S. Richardson, "The timed 'up & G': A test of basic functional mobility for frail elderly persons," *J. Amer. Geriatrics Soc.*, vol. 39, no. 2, pp. 142–148, Feb. 1991, doi: [10.1111/j.1532-5415.1991.tb01616.x](https://doi.org/10.1111/j.1532-5415.1991.tb01616.x).
- [2] M. E. Tinetti, "Performance-oriented assessment of mobility problems in elderly patients," *J. Amer. Geriatrics Soc.*, vol. 34, no. 2, pp. 119–126, Feb. 1986, doi: [10.1111/j.1532-5415.1986.tb05480.x](https://doi.org/10.1111/j.1532-5415.1986.tb05480.x).
- [3] P. W. Duncan, D. K. Weiner, J. Chandler, and S. Studenski, "Functional reach: A new clinical measure of balance," *J. Gerontology*, vol. 45, no. 6, pp. M192–M197, Nov. 1990, doi: [10.1093/geronj/45.6.m192](https://doi.org/10.1093/geronj/45.6.m192).
- [4] B. Thélot, G. Pédrone, and L. Lasbèur, "Epidemiological surveillance of falls in the elderly in France," *Revue d'Épidémiologie et de Santé Publique*, vol. 66, p. S336, Jul. 2018, doi: [10.1016/j.respe.2018.05.263](https://doi.org/10.1016/j.respe.2018.05.263).
- [5] A.-M. Hill et al., "Fall rates in hospital rehabilitation units after individualised patient and staff education programmes: A pragmatic, stepped-wedge, cluster-randomised controlled trial," *Lancet*, vol. 385, no. 9987, pp. 2592–2599, Jun. 2015, doi: [10.1016/s0140-6736\(14\)61945-0](https://doi.org/10.1016/s0140-6736(14)61945-0).
- [6] N. Blanpain and O. Chardon, "Population projections for 2060: One-third of the population aged over 60," Institut Nat. de la Statistique et des Études Économiques (INSEE), Paris, France, INSEE Première 1320, 2010.
- [7] H. Aykan, "Report to congress: Aging services technology study," Office Disab., Aging Long-Term Care Policy, Office Assistant Secretary Planning Eval., U.S.Dept. Health Hum. Services, Washington, DC, USA, Contract HHSP23320095647WC, 2012.
- [8] S. Sourdet, *Recherche Des Causes De Fragilités*. Paris, France: Societe française de gerontologie, 2015, pp. 51–53.
- [9] I. L. Kyrdalen, P. Thingstad, L. Sandvik, and H. Ormstad, "Associations between gait speed and well-known fall risk factors among community-dwelling older adults," *Physiotherapy Res. Int.*, vol. 24, no. 1, p. 1743, Jan. 2019, doi: [10.1002/pri.1743](https://doi.org/10.1002/pri.1743).
- [10] K. Nagai et al., "Near falls predict substantial falls in older adults: A prospective cohort study," *Geriatrics Gerontol. Int.*, vol. 17, no. 10, pp. 1477–1480, Oct. 2017, doi: [10.1111/ggi.12898](https://doi.org/10.1111/ggi.12898).
- [11] Y. Xu, J. Chen, Q. Yang, and Q. Guo, "Human posture recognition and fall detection using Kinect V2 camera," in *Proc. Chin. Control Conf. (CCC)*, Guangzhou, China, Jul. 2019, pp. 8488–8493, doi: [10.23919/ChiCC.2019.8865732](https://doi.org/10.23919/ChiCC.2019.8865732).
- [12] R. Soubra, F. Mourad-Chehade, and A. Chkeir, "Automation of the timed up and go test using a Doppler radar system for gait and balance analysis in elderly people," *J. Healthcare Eng.*, vol. 2023, no. 1, pp. 1–15, Jun. 2023, doi: [10.1155/2023/2016262](https://doi.org/10.1155/2023/2016262).
- [13] G. L. Santos, P. T. Endo, K. H. D. C. Monteiro, E. D. S. Rocha, I. Silva, and T. Lynn, "Accelerometer-based human fall detection using convolutional neural networks," *Sensors*, vol. 19, no. 7, p. 1644, Apr. 2019, doi: [10.3390/s19071644](https://doi.org/10.3390/s19071644).
- [14] S. Illoga, A. Bordat, J. Le Kernec, and O. Romain, "Human activity recognition based on acceleration data from smartphones using HMMs," *IEEE Access*, vol. 9, pp. 139336–139351, 2021, doi: [10.1109/ACCESS.2021.3117336](https://doi.org/10.1109/ACCESS.2021.3117336).
- [15] A. Caronni et al., "Criterion validity of the instrumented timed up and go test: A partial least square regression study," *Gait Posture*, vol. 61, pp. 287–293, Mar. 2018, doi: [10.1016/j.gaitpost.2018.01.015](https://doi.org/10.1016/j.gaitpost.2018.01.015).
- [16] A. Bordat, P. Dobias, J. L. Kernec, D. Guyard, and O. Romain, "GPU based implementation for the pre-processing of radar-based human activity recognition," in *Proc. 25th Euromicro Conf. Digit. Syst. Design (DSD)*, Maspalomas, Spain, Aug. 2022, pp. 593–598, doi: [10.1109/DSD57027.2022.00005](https://doi.org/10.1109/DSD57027.2022.00005).
- [17] G. R. A. Mangano, M. S. Valle, A. Casabona, A. Vagnini, and M. Cioni, "Age-related changes in mobility evaluated by the timed up and go test instrumented through a single sensor," *Sensors*, vol. 20, no. 3, p. 719, Jan. 2020, doi: [10.3390/s20030719](https://doi.org/10.3390/s20030719).
- [18] L. Ruiz-Ruiz, A. R. Jimenez, G. Garcia-Villamil, and F. Seco, "Detecting fall risk and frailty in elders with inertial motion sensors: A survey of significant gait parameters," *Sensors*, vol. 21, no. 20, p. 6918, Oct. 2021, doi: [10.3390/s21206918](https://doi.org/10.3390/s21206918).
- [19] V. Roshdibnam, G. J. Jogerst, N. R. Butler, and S. Baek, "Machine learning prediction of fall risk in older adults using timed up and go test kinematics," *Sensors*, vol. 21, no. 10, p. 3481, May 2021, doi: [10.3390/s21103481](https://doi.org/10.3390/s21103481).
- [20] P. Savoie, J. A. D. Cameron, M. E. Kaye, and E. J. Scheme, "Automation of the timed-up-and-go test using a conventional video camera," *IEEE J. Biomed. Health Informat.*, vol. 24, no. 4, pp. 1196–1205, Apr. 2020, doi: [10.1109/JBHI.2019.2934342](https://doi.org/10.1109/JBHI.2019.2934342).

- [21] C.-Y. Hsieh, H.-Y. Huang, K.-C. Liu, K.-H. Chen, S. J.-P. Hsu, and C.-T. Chan, "Subtask segmentation of timed up and go test for mobility assessment of perioperative total knee arthroplasty," *Sensors*, vol. 20, no. 21, p. 6302, Nov. 2020, doi: [10.3390/s20216302](https://doi.org/10.3390/s20216302).
- [22] C. Béranger et al., "Radar-based human activity acquisition, classification and recognition towards elderly fall prediction," in *Proc. 26th Euromicro Conf. Digit. Syst. Design (DSD)*. Golem, Albania: IEEE, Sep. 2023, pp. 95–102, doi: [10.1109/dsd60849.2023.00023](https://doi.org/10.1109/dsd60849.2023.00023).
- [23] A. Weiss, T. Herman, M. Plotnik, M. Brozgol, N. Giladi, and J. M. Hausdorff, "An instrumented timed up and go: The added value of an accelerometer for identifying fall risk in idiopathic fallers," *Physiological Meas.*, vol. 32, no. 12, pp. 2003–2018, Dec. 2011, doi: [10.1088/0967-3334/32/12/009](https://doi.org/10.1088/0967-3334/32/12/009).
- [24] B. R. Greene, A. O'Donovan, R. Romero-Ortuno, L. Cogan, C. N. Scanaill, and R. A. Kenny, "Quantitative falls risk assessment using the timed up and go test," *IEEE Trans. Biomed. Eng.*, vol. 57, no. 12, pp. 2918–2926, Dec. 2010, doi: [10.1109/TBME.2010.2083659](https://doi.org/10.1109/TBME.2010.2083659).
- [25] A. Ntanis, N. Kostikis, I. Tsimperis, K. Tsioris, G. Rigas, and D. Fotiadis, "Evaluating parameters of the TUG test based on data from IMU and UWB sensors," in *Proc. 18th Int. Conf. Wireless Mobile Comput., Netw. Commun. (WiMob)*, Oct. 2022, pp. 142–147, doi: [10.1109/WiMob55322.2022.9941700](https://doi.org/10.1109/WiMob55322.2022.9941700).
- [26] C. Hadjipanayi and T. G. Constantinou, "Remote gait analysis for assisted living using coherent ultra-wideband radar-on-chip technology," Ph.D. thesis, Imperial College London, London, U.K., 2024.
- [27] A. Dubois, T. Bihl, and J.-P. Bresciani, "Automatic measurement of fall risk indicators in timed up and go test," *Informat. Health Social Care*, vol. 44, no. 3, pp. 237–245, Jul. 2019, doi: [10.1080/17538157.2018.1496089](https://doi.org/10.1080/17538157.2018.1496089).
- [28] M. D. Lewek, C. E. Bradley, C. J. Wutzke, and S. M. Zinder, "The relationship between spatiotemporal gait asymmetry and balance in individuals with chronic stroke," *J. Appl. Biomechanics*, vol. 30, no. 1, pp. 31–36, Feb. 2014, doi: [10.1123/jab.2012-0208](https://doi.org/10.1123/jab.2012-0208).
- [29] K. Paterson, K. Hill, and N. Lythgo, "Stride dynamics, gait variability and prospective falls risk in active community dwelling older women," *Gait Posture*, vol. 33, no. 2, pp. 251–255, Feb. 2011, doi: [10.1016/j.gaitpost.2010.11.014](https://doi.org/10.1016/j.gaitpost.2010.11.014).
- [30] I. Bautmans, B. Jansen, B. Van Keymolen, and T. Mets, "Reliability and clinical correlates of 3D-accelerometry based gait analysis outcomes according to age and fall-risk," *Gait Posture*, vol. 33, no. 3, pp. 366–372, Mar. 2011, doi: [10.1016/j.gaitpost.2010.12.003](https://doi.org/10.1016/j.gaitpost.2010.12.003).
- [31] S. S. Ram, Y. Li, A. Lin, and H. Ling, "Doppler-based detection and tracking of humans in indoor environments," *J. Franklin Inst.*, vol. 345, no. 6, pp. 679–699, Sep. 2008.
- [32] F. Fioranelli, S. A. Shah, H. Li, A. Shrestha, and J. Le Kernec, "Radar signatures of human activities," Univ. Glasgow, Glasgow, U.K., Tech. Rep., 2019, doi: [10.5525/GLA.RESEARCHDATA.848](https://doi.org/10.5525/GLA.RESEARCHDATA.848).
- [33] A. Bordat et al., "Imaging database (radar, event-based camera) of daily movement activities," ETIS Lab, CY Cergy Paris Université/ENSEA/CNRS UMR8051, Cergy Pontoise, France, Tech. Rep., 2023.
- [34] R. C. Gonzalez and R. E. Woods, *Digital Image Processing*, 4th ed., New York, NY, USA: Pearson, 2017.
- [35] J. Serra and J. Serra, *Image Analysis and Mathematical Morphology*, vol. 1, 4th ed., London, U.K.: Academic, 1993.
- [36] T. K. Koo and M. Y. Li, "A guideline of selecting and reporting intraclass correlation coefficients for reliability research," *J. Chiropractic Med.*, vol. 15, no. 2, pp. 155–163, Jun. 2016, doi: [10.1016/j.jcm.2016.02.012](https://doi.org/10.1016/j.jcm.2016.02.012).
- [37] O. Gerke, "Reporting standards for a Bland–Altman agreement analysis: A review of methodological reviews," *Diagnostics*, vol. 10, no. 5, p. 334, May 2020, doi: [10.3390/diagnostics1005034](https://doi.org/10.3390/diagnostics1005034).
- [38] G. Birchley, R. Huxtable, M. Murtagh, R. ter Meulen, P. Flach, and R. Gooberman-Hill, "Smart homes, private homes? An empirical study of technology researchers' perceptions of ethical issues in developing smart-home health technologies," *BMC Med. Ethics*, vol. 18, no. 1, p. 23, Dec. 2017, doi: [10.1186/s12910-017-0183-z](https://doi.org/10.1186/s12910-017-0183-z).
- [39] F. Fioranelli, J. Le Kernec, and S. A. Shah, "Radar for health care: Recognizing human activities and monitoring vital signs," *IEEE Potentials*, vol. 38, no. 4, pp. 16–23, Jul. 2019, doi: [10.1109/MPOT.2019.2906977](https://doi.org/10.1109/MPOT.2019.2906977).
- [40] F. Fioranelli and J. Le Kernec, "Radar sensing for human healthcare: Challenges and results," in *Proc. IEEE Sensors*, Oct. 2021, pp. 1–4, doi: [10.1109/SENSORS47087.2021.9639702](https://doi.org/10.1109/SENSORS47087.2021.9639702).
- [41] D. Carneros-Prado, S. González-Velázquez, C. C. Dobrescu, I. González, J. Fontecha, and R. Hervás, "Automation of observational gait assessment through an optical 3D motion system and transformers," *Appl. Intell.*, vol. 55, no. 4, p. 250, Feb. 2025, doi: [10.1007/s10489-024-06163-w](https://doi.org/10.1007/s10489-024-06163-w).



Alexandre Bordat He received the degree in embedded systems engineering from ENSEA, Cergy, France, in 2021, and the Ph.D. degree from CY Cergy Paris Université, Cergy, in 2025, within the CELL team of the ETIS Laboratory, under a CIFRE contract in collaboration with BlueLinea.

He is a Research and Development Engineer at BlueLinea and a Research Associate at the ETIS Laboratory, UMR, CY Cergy Paris Université, ENSEA, CNRS, Cergy. His research focuses on embedded computing, signal and image processing,

and machine learning, with a particular emphasis on human activity monitoring using radar imaging technologies. His expertise includes time-frequency analysis, mathematical morphology, micro-Doppler signature analysis, and parallel processing on heterogeneous architectures such as CPUs and GPUs.



Claire Béranger received the master's degree in intelligent communicating systems (SIC) from CY Cergy Paris Université, Cergy, France, specialising in Computer Science and Complex Systems Engineering (IISC), with a focus on Artificial Intelligence and Robotics (IAR), where she is currently pursuing the Ph.D. degree. Her Ph.D. thesis focuses on activity recognition and fall risk prediction using deep learning on non-conventional radar data. She develops artificial intelligence-based algorithms and models to recognise the daily activities of elderly or hospitalised people.

She conducts her research at the ETIS laboratory, UMR, CY Cergy Paris Université, ENSEA, CNRS, Cergy. She completed her master's internship at a research institute working on autonomous trains and passenger safety. Her doctoral research is part of the "Paris Région Ph.D.²" program, and co-funded by CY Cergy Paris Université and BlueLinea.



Michel Chapron received the Ph.D. degree from the LAAS-CNRS, Toulouse, France.

He is an Associate Professor at ENSEA and a Researcher at the ETIS Laboratory, UMR, CY Cergy Paris Université, ENSEA, CNRS, Cergy, France. He conducted research in the robotics laboratory on automatic control of electronic components using image processing and shape recognition techniques. He later joined ENSEA and the ETIS Laboratory, where he worked on denoising, multi-scale contour detection in color images, and 3D reconstruction by stereovision. He has also collaborated with several INRAE research centers (Grignon, Dijon, Avignon) on 3D soil reconstruction using stereovision, and on the recognition and classification of weeds in 2D and 3D from color and multispectral images in corn fields. His current research interests include virtual and augmented reality technologies.



Petr Dobias received the degree in electronics from the ENSSAT, the University of Rennes 1, Rennes, France, and dual Master Research degree in electrical engineering and telecommunications from the ISTIC, the University of Rennes 1, where he is currently pursuing the Ph.D. degree, where he worked on his Ph.D. thesis at the Inria, CNRS, IRISA Laboratory, Lannion, France.

He is an Associate Professor at CY Cergy Paris Université and he carries out the research at the Research Laboratory ETIS, UMR, CY Cergy Paris Université, ENSEA, CNRS, Cergy, France. He spent ten months in total at the PARC lab of the University of Auckland, New Zealand, as a visiting student. He was a research and teaching associate at the Sorbonne Université, CNRS, LIP6, Paris, France. Then, he was an Associate Professor at ESIEE-IT, 8 rue Pierre de Coubertin, 95 300 Pontoise and an associate member of ETIS Laboratory. He currently occupies himself with research on the mapping and scheduling, fault tolerance, embedded systems, and neural networks.



David Guyard received the engineering degree in opto and microelectronics from the École Nationale Supérieure d'Ingénieurs de Caen in 1993 and the Ph.D. degree in electronics from the University of Caen, Caen, France, in 1996.

He worked at Philips Consumer Communications from 1996 to 2000, and at French carriers Bouygues Telecom from 2000 to 2006, and SFR from 2006 to 2015, where he honed his expertise in mobile telecommunications, multimedia processing, embedded software, and mobile applications. Since 2015, he has been serving as the Chief Technology Officer at Bluelinea, Versailles, France. His research interests include the development of IoT solutions for healthcare, innovative technologies for elderly care, and smart home systems.



Julien Le Kernec (Senior Member, IEEE) received the B.Eng. and M.Eng. degrees in electronic engineering from the Cork Institute of Technology, Cork, Ireland, in 2004 and 2006, respectively, the Ph.D. degree in electronic engineering from the University Pierre and Marie Curie, Paris, France, in 2011, and the "Habilitation à Diriger des Recherches" from University Cergy-Pontoise, France, in 2022.

He is currently a Senior Lecturer with the School of Engineering in the Autonomous Systems & Connectivity Group, University of Glasgow, he is also an Adjunct Associate Professor at the University Cergy-Pontoise, in the ETIS (Information and Signal Processing Group). Previous to this, he held a post-doctoral position with the Kuang-Chi Institute of Advanced Technology, Shenzhen, China, from 2011 to 2012, and he was a Lecturer at the Department of Electrical and Electronic Engineering, University of Nottingham Ningbo China, from 2012 to 2016.

His research interests include radar system design, software-defined radio/radar, signal processing, and health applications. He has over 140 publications in journals (IEEE SENSORS, IEEE Signal Processing Magazine, IEEE JOURNAL OF BIOMEDICAL AND HEALTH INFORMATICS, NATURE SCIENTIFIC REPORTS), Conferences (IET International Radar Conference, IEEE Radar Conference), book chapters, patents and databases.



Olivier Romain received the M.S. degree in electronics from Louis Pasteur University, Paris, France, the Ph.D. degree in electronics from University Pierre and Marie Curie (UPMC), Paris, and the Habilitation degree in electronics from UPMC.

His teaching qualification (agrégation) in electronics from the École Normale Supérieure de Cachan, France. Since 2011, he is a Full Professor of electrical and computer science at Cergy Paris University - CYU, France. He conducts research activities in the field of smart embedded systems for health care, the Internet of Things, and security.